ChemPhysChem

Research Article
doi.org/10.1002/cphc.202200648

Chemistry Europe
European Chemical Societies Publishing

www.chemphyschem.org

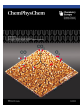

Highly Ordered and Thermally Stable FeRh Cluster Superlattice on Graphene for Low-Temperature Catalytic CO Oxidation

Hao Yin,*[a] Jean-Guillaume de Groot,[a] and Harald Brune*[a]

We report on bimetallic FeRh clusters with a narrow size-distribution grown on graphene on Ir(111) as a carbon-supported model catalyst to promote low-temperature catalytic CO oxidation. By combining scanning tunneling microscopy with catalytic performance measurements, we reveal that Fe–Rh interfaces are active sites for oxygen activation and CO oxidation, especially at low temperatures. Rh core Fe shell clusters not only provide the active sites for the reaction, but also thermally stabilize surface Fe atoms towards coarsening compared with pure Fe clusters. Alternate isotope-labelled CO/O_2 pulse experiments show opposite trends on preferential oxidation (PROX) performance because of surface hydroxyl species formation and competitive adsorption between CO and O_2. The present results introduce a general strategy to stabilize metallic clusters and to reveal the reaction mechanisms on bimetallic structures for low-temperature catalytic CO oxidation as well as preferential oxidation.

Introduction

The classical CO oxidation on Pt group metals (PGMs, such as Pt, Rh, Ir, Pd, Ru) has been studied for decades since Langmuir's pioneering work in 1922,[1] and PGM-based catalytic converters are commonly applied in exhaust systems. Even though the Eley–Rideal[2,3] mechanism has been reported in some cases, the Langmuir–Hinshelwood mechanism[4,5] dominates most PGM catalysts for the CO oxidation reaction. The Langmuir–Hinshelwood mechanism involves molecular CO adsorption, dissociative O_2 adsorption, and further reaction of CO_{ads} with O_{ads} to form CO_2 that desorbs. Due to the strong affinity between CO and PGMs, the catalytic performance at room temperature is limited as the PGM surfaces become poisoned by adsorbed CO, which inhibits the adsorption and dissociation of O_2.[6] Although PGM catalysts may reach almost 100 % conversion rate above the CO desorption temperature of 600 K, industry still suffers from the low reactivity at low-temperature, especially for exhaust gas treatment, from performance degradation due to catalyst sintering at higher temperatures, and from competing reactions at H_2-rich atmosphere (preferential oxidation – PROX). Several strategies have been developed to promote low-temperature CO oxidation by weakening the metal-CO interaction or/and encouraging O_2 dissociation such as introducing exotic oxide and hydroxide support,[7] tuning cluster sizes even down to the single-atom level,[8–10] and developing other metal systems (Au clusters,[11,12] bimetallic alloys,[13,14] *etc.*).

Due to particular affiliation with oxygen, coordinatively unsaturated metallic iron or ferrous/PGM interfaces exhibit promising performance in low-temperature CO oxidation and PROX. Bao *et al.*[15] have shown that the Pt–Fe interface confinement effect can facilitate CO oxidation with unsaturated Fe sites on a FeO_{1-x}/Pt(111) model system prepared in ultra-high vacuum (UHV). Zheng *et al.*[16] reported that Fe^{3+}–OH–Pt interfaces readily react with CO adsorbed nearby to directly yield CO_2 and simultaneously produce coordinatively unsaturated Fe sites for O_2 activation. Further, Lu *et al.*[17] have found that even $Fe_1(OH)_x$–Pt single interfacial sites can readily react with CO and facilitate oxygen activation on atomic layer deposition prepared nanoparticles. These studies manifest the influence of the interfacial structure of the bi-metallic catalysts on their catalytic activity and on the reaction mechanisms.

The surface science approach to heterogeneous catalysis, based on UHV characterized single-crystal surfaces as model catalysts, has successfully unraveled several important reaction behaviors since the 80s, where one of the well-known works is the oscillatory kinetics in CO oxidation revealed by photoelectron emission microscopy (PEEM).[18] Since then the research has focused on UHV-prepared model systems that minimize the gap with real industrial catalysis including both catalyst design and reaction conditions.[19,20] In many cases, industrial heterogeneous catalysts consist of metallic particles (<10 nm) dispersed on supporting materials (carbon, oxides, zeolite, *etc.*) making mono-dispersed metallic cluster/support realistic UHV model systems. As model of commercial metal/carbon catalysts, graphene (Gr) on lattice-mismatched Ir(111) is an ideal carbon support since it enables the self-assembly of metal clusters

[a] *Dr. H. Yin, Dr. J.-G. de Groot, Prof. Dr. H. Brune*
Institute of Physics,
École Polytechnique Fédérale de Lausanne (EPFL),
1015 Lausanne, Switzerland
E-mail: hao.yin@epfl.ch
harald.brune@epfl.ch

Supporting information for this article is available on the WWW under https://doi.org/10.1002/cphc.202200648

grown on top the *hcp* stacking areas of the (9.32×9.32) moiré pattern.[21–25]

For this work, we prepared pure Rh and Fe, as well as FeRh bimetallic cluster superlattices on Gr/Ir(111) by deposition at cryogenic temperatures. Variable-temperature scanning tunneling microscopy (VT-STM) reveals the morphology and thermal stability of the clusters. FeRh clusters are thermally much more stable than pure Fe clusters and FeRh alloy clusters can be created without coarsening. Temperature-dependent changes in the surface adsorbed species as a result of competitive CO and O* adsorption are revealed by alternate CO/O_2 pulse experiments. We show that FeRh alloy clusters promote low-temperature CO oxidation (onset temperature at 320 K) and PROX, which benefit from O_2 activation at Fe/Rh interface sites. The size distributions obtained by self-assembly are so narrow that the present experiments come close to the ones on size-selected clusters[9,26,27] at surfaces as model catalysts.

Results and Discussion

We create the metal cluster superlattice by self-assembly on the (9.32×9.32) moiré pattern formed by graphene on Ir(111).[21,22] This template surface exhibits excellent long-range order, as demonstrated in Figure S1. The moiré structure involves a periodic and smooth variation of the graphene registry with respect to the underlying Ir(111) surface, leading to a periodic variation of its binding energy to the substrate and its vertical distance from it. For metal atoms deposited on-top of graphene, this creates a periodic variation of their binding energy, involving for some metals in the strongest binding graphene areas, that are *hcp*-stacked with respect to Ir(111), an sp^2 to sp^3 re-hybridization of the carbon atoms.[23] During deposition, adatoms accumulate in this area of the moiré unit cell where they create one nucleus. Below a certain size, and depending on the deposition temperature, these nuclei might be mobile. However, their most favorable site is the one where they formed. During further deposition, the nuclei grow to clusters, yielding equally spaced clusters with a narrow size distribution and thus an ideal model system for heterogeneous catalysis. It allows to address the size-dependence of the catalytic performance and to identify the active sites. The self-assembly of metal cluster superlattices on Gr/Ir(111) has first been demonstrated for Ir,[22] and then for other metal atoms including Rh[24] and Fe[25] used here. However, the growth of core-shell Rh-seeded Fe clusters, of FeRh alloy clusters, and of well-ordered pure Fe clusters, have not been reported before.

Figure 1 shows STM images of the close-packed 0.3 monolayer (ML) Fe, 0.18 ML Rh, and FeRh (0.18 ML Rh + 0.08 ML Fe) clusters on Gr/Ir(111) after the indicated annealing temperatures. At 300 K, in all three cases, the clusters are close to mono-disperse and form an almost perfect superlattice. The filling of moiré cells is close to 90% for Fe and around 80% for Rh. The mean cluster sizes, as concluded from the deposited amount and the filling of moiré cells, are 26 atoms for Fe and 19 atoms for Rh. The order achieved for pure Fe is remarkable and requires the cryogenic deposition temperature of 50 K, as deposition at 300 K gives no order at all.[21,25] For Rh, the best order was achieved for the shown deposition temperature of 130 K, which is slightly higher than the 90 K used in reference.[24]

The thermal stability of the clusters can be inferred from visual inspection of the STM images in Figure 1, combined with the apparent height histograms in Figure S2. For the Fe clusters, the first change occurs in the apparent height distribution at 500 K annealing temperature, where it extends to larger heights. This change is also perceived in the STM images, showing fewer and higher clusters from $T_{ann} = 500$ K onward. For Rh, the apparent height histograms remain to a good approximation unchanged up to 500 K, and coarsening sets in only at 600 K. We attribute the higher stability of Rh to the larger cohesive energy of this element, preventing Ostwald ripening. In addition, the energy barrier for the diffusion of entire clusters on the graphene moiré pattern must be larger for Rh than for Fe, preventing Smoluchowski ripening. The larger initial apparent heights observed for Fe clusters suggest that they are double layer while Rh clusters are single layer. Therefore, the Fe clusters have a smaller footprint at equivalent mean size which would explain their earlier ripening. Fe clusters with significantly improved thermal stability are created by Rh seeding. As seen from Figure 1, their ripening starts only at $T_{ann} = 600$ K. In order to avoid thermal ripening, we limited our CO oxidation study to 500 K.

To estimate the *d*-band filling of the respective cluster surfaces, we conducted temperature-programmed N_2 desorption (N_2-TPD) experiments. With the existence of $d \rightarrow 2\pi^*$ back-donation and $\sigma \rightarrow d$ donation, the N_2 adsorption energy to the surface metal atoms is closely related to the surface electronic structure.[28] Due to the difference in electronegativity between Fe and Ir(Rh), Fe is expected to donate electrons to Ir(Rh) at the respective boundary, which weakens the Fe–N_2 binding energy. For the cluster/Gr/Ir system, graphene as the separation layer is well known to prevent electron transfer between clusters and substrate,[29] which is another advantage for designing a metal/carbon model system. As shown in Figure 2, the Fe–N_2 binding energy for Fe/Ir (light green) is considerably lower than the one for Fe clusters on Gr/Ir(111) (dark green) as expressed in the decrease of T_{des} from 120 K to 90 K. While the Fe clusters are very likely 2 layers high, the Fe islands on Ir are one monolayer high. Also, the Fe clusters have more low-coordinated atoms than the larger 2D islands. Hence, structural differences add to the electronic ones. However, there is a single desorption peak for both systems, while each of them exhibits atomic Fe sites with different coordination. Therefore, we conclude that the dominant effect causing the 30 K shift in T_{des} is not the structure but an electronic difference, Fe donates electrons to Ir, while it is well separated from the metal substrate on graphene. As expected, for the sample with coexisting Fe/Ir and Fe/Gr/Ir clusters (red), both desorption peaks are present. For FeRh bimetallic clusters (yellow), two desorption peaks at 90 K and 150 K appear which match with N_2 desorption from Fe/Ir and Rh/Gr/Ir (black) respectively. Thus, Fe wetting Rh clusters has similar N_2 binding energy as Fe monolayer islands on Ir(111), and the 150 K peak is reminiscent of clean Rh surface parts of

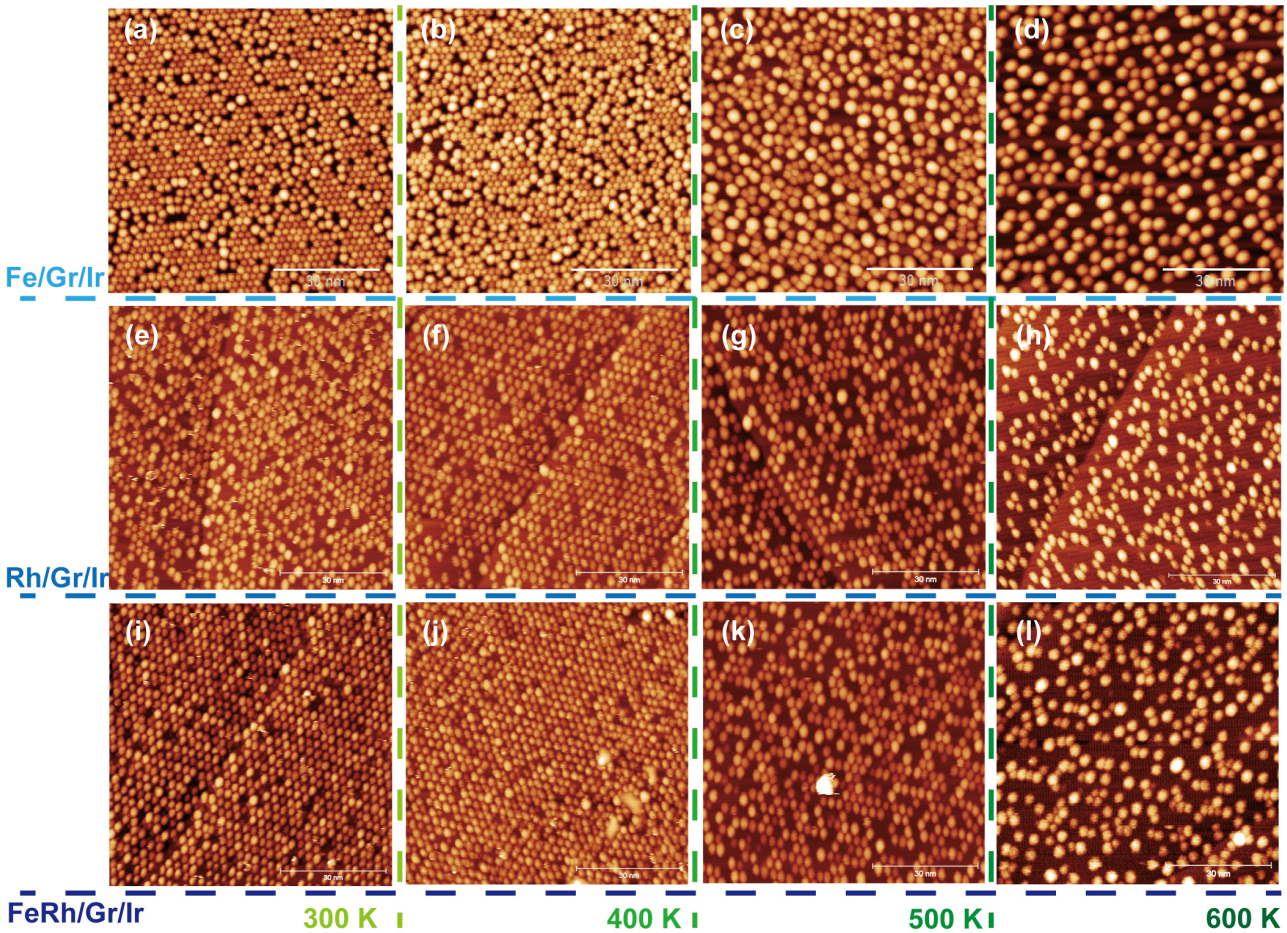

Figure 1. Constant current STM images of 0.3 ML Fe (a–d), 0.18 ML Rh (e–h), and 0.18 ML Rh + 0.08 ML Fe (i–j) clusters on graphene on Ir(111) ($V_t = 1050$ mV, $I_t = 1.0$ nA, 80 nm × 80 nm) after annealing to 300–600 K. T_{dep}(Fe) = 50 K, T_{dep} (Rh) = 130 K, and T_{dep} (FeRh) = 130 K.

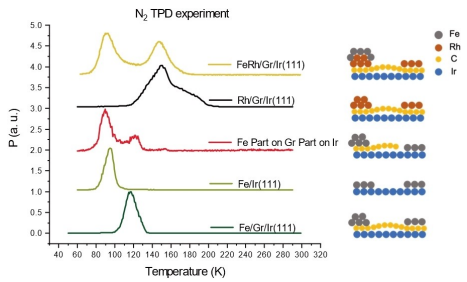

Figure 2. N_2-TPD experiment on Fe/Gr/Ir, Fe/Ir, a mixture of Fe/Gr/Ir and Fe/Ir, Rh/Gr/Ir, and FeRh/Gr/Ir with 0.005 L N_2 dose at 50 K. The heating rate is 1 K/s.

the seed clusters that are not entirely wetted by Fe. From the respective coverages, the 19 atom Rh seed cluster has on average 8 Fe atoms, however, since the wetting is inhomogeneous, some Rh seed clusters have less than 8 Fe atoms, explaining the significant amount of remaining clean Rh surface sites.

To address potential changes in the surface composition caused by annealing, we performed N_2-TPD after annealing the clusters to different temperatures (Figure S3). For pure Fe clusters, there is a single desorption peak at 120 K for annealing up to 400 K, consistent with their thermal stability reported above. Upon annealing at 500 K, a second desorption peak at 98 K appears that we attribute to another adsorption site appearing once the clusters become more than 2 layers high. For FeRh bimetallic clusters, the desorption peak at ~90 K (N_2 on Fe shell) gradually decreases with increasing T_{ann}, and a broad peak appears at ~170 K upon annealing to 500 K, where the clusters don't ripen much, according to Figures 1(i ~ l). This change in surface chemical composition is attributed to a transition from core-shell structure to alloy clusters setting in at $T_{ann} = 500$ K. Note that this transition takes place largely preserving the superlattice structure. At $T_{ann} = 600$ K, the clusters coarsen significantly, reflected by the TPD peak further changing its shape.

To evaluate the catalytic performance of UHV-prepared metal clusters, we employed a home-built chemical analyzer (Sniffer).[30,31] It allows us to dose gas pulses selectively to the surface and to analyze the reaction products with QMS (Figure 3a). For the present UHV-chamber, we implemented a linear travel along its axis and mounted the Sniffer onto a CF 150 flange, formerly hosting a LEED system. For catalytic CO

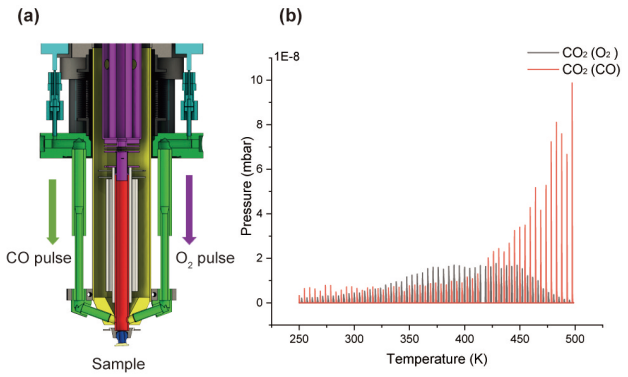

Figure 3. (a) Schematic longitudinal cut of the chemical analyzer (Sniffer) (b) CO_2 production vs. temperature on Rh/Gr/Ir synchronized with CO/O_2 pulses to reveal CO_{ad} rich and O_{ad} rich reaction regimes. The heating rate is 0.5 K/s.

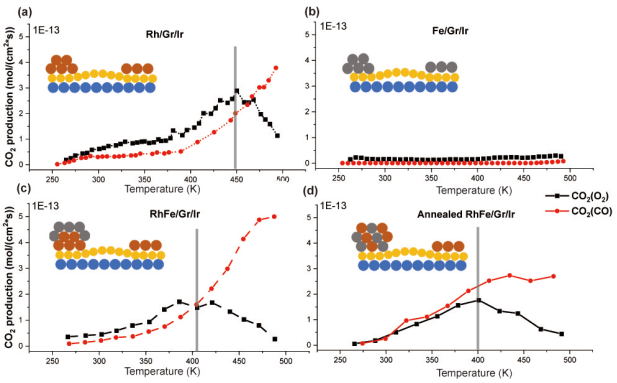

Figure 4. Catalytic CO oxidation performance as a function of temperature for Rh/Gr/Ir (a), Fe/Gr/Ir (b), core-shell RhFe/Gr/Ir (c), and RhFe alloy clusters on Gr/Ir (d), obtained by annealing the core-shell clusters to 500 K. For clarity, we don't show the individual pulses but only their heights. $CO_2(CO)$ is shown in red and $CO_2(O_2)$ in black. The amount of CO and O_2 per pulse is 0.2 L.

oxidation, we alternately dosed 0.2 L isotope-labelled $^{13}C^{16}O$ ($m/z=29$) and $^{18}O_2$ ($m/z=36$) pulses onto the sample while applying a linear temperature ramp (Figure 3 shows the example of Rh/Gr/Ir). We analyzed the amount of $^{13}C^{16}O^{18}O$ ($m/z=47$) synchronized with the CO (red) and with the O_2 pulse (black). Below 300 K, we observe weak CO_2 production due to CO_{ad} saturating the Rh clusters preventing O_2 dissociation, which is the well-known CO poisoning at low temperature[32,33] (Figures 3 and 4a). $CO_2(O_2)$ production increases from 300 K, where CO starts to desorb from the Rh surface and leaves active sites for oxygen dissociation, which is confirmed by CO TPD results (Figure S4). The maximum of $CO_2(O_2)$ is observed at roughly 380–450 K, because of the optimum balance between the remaining CO_{ad} and adsorbing O_2, which can be regarded as competitive adsorption. Thus, the temperature with a maximum of $CO_2(O_2)$ production is sensitive to both CO and dissociative O_2 adsorption rates. With higher CO/O_2 ratios, the maximum of CO_2(O2) appears at higher temperature (Figure S5). Once above 420 K, O_{ad} gradually becomes the dominant species, and CO_2 production is related to the amount of surface CO. Therefore $CO_2(CO)$ starts to increase, while $CO_2(O_2)$ decreases since there is less remaining CO_{ad}. The observed reaction rate as a function of temperature and reactants is very similar to the behaviors on single-crystal surfaces[34] and on industrial[35] catalysts with higher reactant pressure.

Metallic Fe and ferrous sites[15] are recognized to promote dissociative oxygen adsorption which benefits CO oxidation at low-temperature on Pt group metals. Figure 4 compares the reaction product (CO_2) peak heights, and thereby the catalytic performance, of the four investigated cluster compositions as a function of temperature. Due to the weak interaction of CO with pure Fe, the catalytic performance for Fe/Gr/Ir is negligible (Figure 4b) compared with Rh (Figure 4a). The bimetallic clusters significantly reduce the effect of CO poisoning and thereby enable low-T CO oxidation. While the pure Rh clusters show no $CO_2(CO)$ production until 400 K, $CO_2(CO)$ production sets in at 350 K for RhFe/Gr/Ir core-shell clusters (Figure 4c) and starts with 320 K at even lower temperatures for RhFe alloy clusters (Figure 4d). Concomitantly with the reduction of these $CO_2(CO)$ onset temperatures, the maxima of the $CO_2(O_2)$ production, indicated by the gray vertical bars in Figure 4, shift to lower temperatures, *e.g.*, from 450 K to 400 K in going from pure Rh to Fe@Rh-core and alloyed FeRh. The peak of the CO_2 production related to O_2 results from the competitive adsorption between O_{ad} and CO[36] where the surface changes from CO-rich to O-rich. The optimum performance of the catalyst is found between O-rich and CO-rich surfaces, *i.e.*, at temperatures where the $CO_2(O_2)$ production has its maximum.

The turn-over rates at 400 K are significantly different for the three catalytically active cluster species. There are around 3.6×10^{-3} $CO_2(CO)$ molecules generated per cluster per second for Rh/Gr/Ir. This number increases to 5.4×10^{-3} for RhFe core-shell clusters and goes further up to 9.1×10^{-3} for the RhFe alloy clusters. The amount of CO_2 during CO pulses is related to remaining active oxygen species on the surface which are generated during the preceding oxygen pulse. For bimetallic core-shell clusters, we estimate that at low temperature, the Fe part facilitates dissociative oxygen adsorption, and the Rh part of the cluster surface provides adsorption sites for CO. At the interface between the two elements, O_{ad} and CO_{ad} react to form CO_2. As mentioned, after annealing at 500 K, the RhFe core-shell clusters restructure to form alloy clusters. They exhibit more sites where Fe atoms interface Rh atoms at the surface explaining the highest turn-over rate. When alloy clusters were intentionally oxidized (1×10^{-6} mbar O_2 at 600 K),[15] the reactivity was remarkably lower than just annealing to 600 K in UHV (Figure S6), as a result of the oxidation (deactivation) of ferrous sites. We conclude that molecular oxygen is easier dissociated at the RhFe interface within a cluster and thereby undermines the CO poisoning effect, enabling CO oxidation at low temperatures. We now turn to preferential oxidation since the competition between CO and H_2 gives further insight into the reaction dynamics.

CO PROX reactions were conducted with a certain amount of deuterium (D_2) in the residual gas of the UHV chamber. Figure 5 displays the corresponding PROX and catalytic oxida-

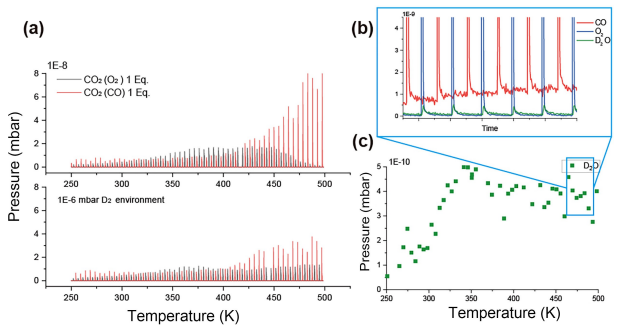

Figure 5. (a) Pulse-synchronized CO_2 production from Rh/Gr/Ir without (upper) and with (bottom) hydrogen in the residual gas. (b)(c) The isotope water D_2O^{18} is only generated during O_2 pulses.

tion performance for Rh/Gr/Ir. Above 400 K, CO_2(CO, PROX) production is less than CO_2(CO) production. Between 350 and 450 K, also the CO_2(O_2, PROX) conversion slightly decreased. On the contrary, the CO_2(O_2) performance with the coexistence of D_2 remarkably increased at 500 K. The $D_2{}^{18}O$ (m/z = 22, green) production synchronized with O_2 (blue) and CO (red) pulses are shown in Figure 5b and 5c. Water is only produced during O_2 pulses. The D_2 oxidation starts at 300 K and reaches its maximum from 350 K on, where it starts to compete with CO oxidation. Surprisingly, if we only take desorbed water as the main product of D_2 oxidation into consideration (the water desorption temperature on iron oxides is below 300 K[37]), the selectivity of CO_2(O_2, PROX) could reach > 95% at 400 K, while the activity decreased more than 30% compared with CO_2(O_2). We, therefore, conclude that besides direct hydrogen competition reaction with CO, the formation of surface hydroxyl species might also contribute to the observed phenomena.

At a certain temperature and pressure, the CO_2(O_2) production is related to a few factors, including the amount of adsorbed CO from CO pulses (N_{CO}), the number of O_2 adsorption sites ($N_{a\text{-}O2} \propto 1/N_{CO}$), the O_2 dissociation rate (K_{dis}), and the number of O adatoms ($N_o \propto N_{a\text{-}O2} \times K_{dis}$). For PROX at 400 K on Rh, we estimated that a fraction of O adatoms reacted with hydrogen instead of CO and generated hydroxyl and water, where relatively strong-binding hydroxyl species (M–OHx)[38] further blocked O_2 adsorption sites, which eventually suppressed the CO_2 production. It is worth to mention that even though as reported,[39,40] M–OHx species may facilitate generating bicarbonates on metal/oxides system, we expect it may not play a significant role in our systems for two reasons. First, carbon supports are much less reactive to oxygen compared with reductive oxide supports, such as TiO_2 or CeO_2. Second, during O_2 pulses, the amount of surface adsorbed CO is limited. The main reason for a poor CO_2(O_2) performance at 500 K is the lack of adsorbed CO (N_{CO}) partially resulting from the competitive adsorption with O_2 as mentioned above (Figure S5). For PROX, due to suppressed O_2 dissociation on the surface, there are more adsorbed CO molecules before the O_2 pulse, which explains the relatively high CO_2(O_2, PROX) production at 500 K. We assume that if we further increased the temperature, the CO_2(O_2, PROX) would eventually vanish due to the CO desorption rate being far beyond its adsorption rate, however, we can't reach those temperatures without inducing coarsening in the clusters. Similar, CO_2(CO) is related to the remaining oxygen adatoms during the O_2 pulse, and the performance gradually decreased due to the formation of hydroxyl species, even without any water generation.

Similar results were also found for bimetallic FeRh alloy clusters, as presented in Figure 6. Compared with a non-hydrogen environment in Figure 6a, RhFe alloy clusters exhibit more sensitivity to H_2 partial pressure below 350 K, where the CO_2(O_2, PROX) production (in Figure 6b) clearly drops even under very small amounts of H_2 (0.04 equivalent). We realize that the high sensitivity comes from the fact that competitive H_2 oxidation only occurs during O_2 pulses. Yet, the CO_2(CO, PROX) performance remained until 350 K, when the production starts to degrade depending on the partial pressure of H_2(D_2), especially at a higher temperature. High-temperature CO_2(CO, PROX) production was significantly reduced when the H_2 partial pressure reached 0.5 *Eq.* For example, CO_2(CO, PROX) production at 450 K in Figure 6c (0.5 *Eq.* H_2) is merely half the one of Figure 6a (0 *Eq.* H_2). Different from the phenomena during O_2 pulses, we conclude that the formation of surface hydroxyl/water species partially remaining on the surface occupying the adsorption sites for oxygen dissociation and further decreasing surface oxygen adatoms in the next CO pulse cause the lower CO_2(CO, PROX) performance (Figure 6c). We further performed measurements at much higher PROX CO ratios, namely at $O_2:CO:H_2 = 0.05:0.05:1$ (Figure 6d), where the CO_2 production was multiplied by 20 to be compared to the other measurements. Even though the CO_2(O_2) production became negligible (Figure S7), temperature-dependent CO_2(CO) showed a similar low-high-low performance in Figure 6d. The results indicate that in an H_2-rich atmosphere, dissociated oxygen adatoms prefer to react with H_2 instead of surface adsorbed CO during O_2 pulses, after which remaining oxygen further oxidates fresh CO during CO pulses which is similar to other CO_2(CO, PROX) processes.

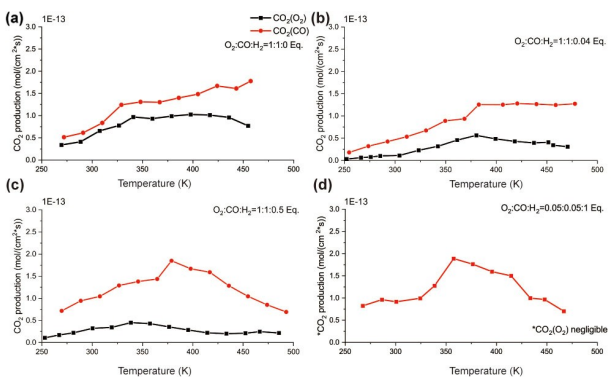

Figure 6. Preferential oxidation performance monitored as CO_2 production correlated with CO and O_2 pulses on RhFe alloy clusters on Gr/Ir with the same color code as in Figure 4. The variable between subfigures is the background pressure of H_2. The amount of CO/O_2 per pulse is $0.5*10^{-6}$ mbar (~0.1 L) in a, b, c and $2.5*10^{-8}$ mbar in d.

Conclusions

In summary, we have conducted a systematic UHV study to elucidate the relevance of the Fe–Rh interface on catalytic CO oxidation and PROX performance on dense-packed metallic clusters/graphene model systems. These thermally stable, equally spaced, and almost monodisperse clusters were self-assembled by templated growth on the moiré pattern formed by graphene on Ir(111). Catalysis measurements performed by alternatingly pulsing CO and O_2 and simultaneously heating the sample from 300 K to 500 K reveal that the CO_2 production at 400 K of FeRh alloy clusters is 2.5 times higher than that of Rh clusters, and 1.6 times higher than that of RhFe core-shell clusters. We attribute this to surface unsaturated Fe–Rh sites promoting oxygen dissociation and this way undermining the CO poisoning effect, especially at low-temperature and generating Fe–O* species that react with CO adsorbed on Rh. We find first CO_2(CO) production already at 320 K. We also demonstrated that hydrogen hinders CO_2(CO) production but promotes CO_2(O_2) performance at 500 K, not only resulting from the participation as a competing reaction but also from the creation of surface hydroxyl species which block O_2 adsorption sites and mediate the CO/O_2 surface concentration. Based on these results, we have a clear understanding of the reaction mechanisms. We find that the bimetallic interfaces strongly affect the catalytic CO oxidation by activating oxygen and by partitioning the adsorption sites amongst the two metals, with CO molecules mainly adsorbing on Rh and O_2 molecules mainly dissociating on Fe.

Experimental Section

Experiments were carried out in an ultra-high vacuum (UHV) variable-temperature STM chamber with a base pressure in the low 10^{-10} mbar range, equipped with a QMS, an e-beam evaporator, a sputter gun, and a gas doser system for ethylene (C_2H_4) and D_2 directed onto the sample surface. A sample manipulator allows for sample heating by electron bombardment, as well as for sample cooling down to 40 K by LHe, and to 130 K by LN_2. The Ir(111) substrate was cleaned by repeated cycles of annealing to 1500 K (1 min) and sputtering with a beam of 1.5 keV 3.1 nA/cm^2 Ar^+ ions at 300 K. Its cleanliness, as well as the density of structural defects, were controlled by means of STM. Graphene was prepared through exposure of the substrate to $5*10^{-7}$ mbar ethylene at 1400 K for 100 seconds. This exposure ensures a saturation coverage of one full graphene monolayer. We calibrated the Fe and Rh deposition rates by determining the fractional coverage from STM images recorded after submonolayer disposition of both elements for a given time onto the clean Ir(111) surface. We define one monolayer (ML) coverage as one Fe or Rh atom per Ir(111) surface atom. The reactant gas dosing and reaction product detection system (Sniffer) was built by equipping a commercial QMS (QMA 200, Pfeiffer Vacuum) with a modified ionizer and a detection volume directly connected to the sample surface. The reactant gas pulses are generated with electrovalves operated by a rectangular voltage pulse of typically 1–4 μs duration and 20–30 V amplitude, corresponding to a partial opening of the valve. For further information, the reader may refer to the description of a former version of the sniffer.[30]

Acknowledgements

Support from the Swiss National Science Foundation under projects 200020_157081/1 and 200020_157081/2 is gratefully acknowledged.

Conflict of Interest

The authors declare no conflict of interest.

Data Availability Statement

The data that support the findings of this study are openly available in zenodo at https://doi.org/10.5281/zenodo.6793469, reference number 6793469.

Keywords: CO oxidation · PROX · UHV-STM · bimetallic catalysts · competitive adsorption

[1] I. Langmuir, *Trans. Faraday Soc.* **1922**, *17*, 621–654.
[2] Z. Duan, G. Henkelman, *ACS Catal.* **2014**, *4*, 3435–3443.
[3] C. H. F. Peden, D. W. Goodman, M. D. Weisel, F. M. Hoffmann, *Surf. Sci.* **1991**, *253*, 44–58.
[4] B. L. M. Hendriksen, S. C. Bobaru, J. W. M. Frenken, *Surf. Sci.* **2004**, *552*, 229–242.
[5] M. E. Domagala, C. T. Campbell, *Catal. Lett.* **1991**, *9*, 65–70.
[6] A. D. Allian, K. Takanabe, K. Fujdala, X. Hao, T. Truex, J. Cai, C. Buda, M. Neurock, E. Iglesia, *J. Am. Chem. Soc.* **2011**, *133*, 4498–4517.
[7] M. Cargnello, V. Doan-Nguyen, T. Gordon, R. Diaz, E. Stach, R. Gorte, P. Fornasiero, C. Murray, *Science* **2013**, *341*, 771–773.
[8] B. Qiao, A. Wang, X. Yang, L. Allard, Z. Jiang, Y. Cui, J. Liu, J. Li, T. Zhang, *Nat. Chem.* **2011**, *3*, 634–641.
[9] S. Bonanni, K. Aït-Mansour, W. Harbich, H. Brune, *J. Am. Chem. Soc.* **2014**, *136*, 8702–8707.
[10] E. J. Peterson, A. T. DeLaRiva, S. Lin, R. S. Johnson, H. Guo, J. T. Miller, J. Hun Kwak, C. H. Peden, B. Kiefer, L. F. Allard, F. H. Ribeiro, A. K. Datye, *Nat. Commun.* **2014**, *5*, 4885.
[11] A. A. Herzing, C. J. Kiely, A. F. Carley, P. Landon, G. Hutchings, *Science* **2008**, *321*, 1331–1335.
[12] G. R. Bamwenda, S. Tsubota, T. Nakamura, M. Haruta, *Catal. Lett.* **1997**, *44*, 83–87.
[13] S. Alayoglu, A. U. Nilekar, M. Mavrikakis, B. Eichhorn, *Nat. Mater.* **2008**, *7*, 333–338.
[14] H. Xu, Q. Fu, Y. Yao, X. Bao, *Energy Environ. Sci.* **2012**, *5*, 6313–6320.
[15] Q. Fu, W. Li, Y. Yao, H. Liu, H. Su, D. Ma, X. Gu, L. Chen, Z. Wang, H. Zang, B. Wang, X. Bao, *Science* **2010**, *328*, 1141–1144.
[16] G. Chen, Y. Zhao, G. Fu, P. N. Duchesne, L. Gu, Y. Zheng, X. Weng, M. Chen, P. Zhang, C. Pao, J. Lee, N. Zheng, *Science* **2014**, *344*, 495–499.
[17] L. Cao, W. Liu, Q. Luo, R. Yin, B. Wang, J. Weissenrieder, M. Soldemo, H. Yan, Y. Lin, Z. Sun, C. Ma, W. Zhang, S. Chen, H. Wang, Q. Guan, T. Yao, S. Wei, J. Yang, J. Lu, *Nature* **2019**, *565*, 631–635.
[18] S. Nettesheim, A. von Oertzen, H. H. Rotermund, G. Ertl, *J. Chem. Phys.* **1993**, *98*, 9977.
[19] H. Freund, *J. Am. Chem. Soc.* **2016**, *138*, 8985–8996.
[20] B. Böller, K. M. Durner, J. Wintterlin, *Nat. Catal.* **2019**, *2*, 1027–1034.
[21] A. T. N'Diaye, J. Coraux, T. N. Plasa, C. Busse, T. Michely, *New J. Phys.* **2008**, *10*, 043033.
[22] A. T. N'Diaye, S. Bleikamp, P. J. Feibelman, T. Michely, *Phys. Rev. Lett.* **2006**, *97*, 215501.
[23] P. J. Feibelman, *Phys. Rev. B* **2008**, *77*, 165419.
[24] A. Cavallin, M. P ozzo, C. Africh, A. Baraldi, E. Vesselli, C. Dri, G. Comelli, R. Larciprete, P. Lacovig, S. Lizzit, D. Alfè, *ACS Nano* **2012**, *6*, 3034–3043.
[25] A. T. N'Diaye, T. Gerber, C. Busse, J. Myslivecek, J. Coraux, T. Michely, *New J. Phys.* **2009**, *11*, 103045.
[26] E. C. Tyo, S. Vajda, *Nat. Nanotechnol.* **2015**, *10*, 577.

[27] U. Heiz, W. D. Schneider, *Crit. Rev. Solid State Mater. Sci.* **2001**, *26*, 251–290.
[28] B. Hammer, Y. Morikawa, J. K. Nørskov, *Phys. Rev. Lett.* **1996**, *76*, 2141–2144.
[29] R. Baltic, M. Pivetta, F. Donati, C. Wäckerlin, A. Singha, J. Dreiser, S. Rusponi, H. Brune, *Nano Lett.* **2016**, *16*, 7610–7615.
[30] S. Bonanni, K. Aït-Mansour, M. Hugentobler, H. Brune, W. Harbich, *Eur. Phys. J. D* **2011**, *63*, 241–249.
[31] J. G. de Groot, PhD thesis: *An Experimental Setup for Heterogeneous Catalysis on Atomically Defined Metal Nanostructures*, École Polytechnique Fédérale de Lausanne (Switzerland), **2021**.
[32] H. Guan, J. Lin, B. Qiao, X. Yang, L. Li, S. Miao, J. Liu, A. Wang, X. Wang, T. Zhang, *Angew. Chem. Int. Ed.* **2016**, *55*, 2820–2824.
[33] D. A. J. M. Ligthart, R. A. van Santen, E. J. M. Hensen, *Angew. Chem. Int. Ed.* **2011**, *50*, 5306–5310.
[34] C. T. Campbell, G. Ertl, H. Kuipers, J. Segner, *J. Chem. Phys.* **1980**, *73*, 5862–5873.
[35] D. W. Goodman, *Surf. Sci.* **1994**, *299–300*, 837–848.
[36] R. M. Ziff, E. Gulari, Y. Barshad, *Phys. Rev. Lett.* **1986**, *56*, 2553–2556.
[37] E. Zaki, Z. Jakub, F. Mirabella, G. S. Parkinson, S. Shaikhutdinov, H. J. Freund, *J. Phys. Chem. Lett.* **2019**, *10*, 2487–2492.
[38] J. Saavedra, H. A. Doan, C. J. Pursell, L. C. Grabow, B. D. Chandler, *Science* **2014**, *345*, 1599–1602.
[39] M. M. Schubert, A. Venugopal, M. J. Kahlich, V. Plzak, R. J. Behm, *J. Catal.* **2004**, *222*, 32–40.
[40] A. Davó-Quiñonero, M. Navlani-García, D. Lozano-Castelló, A. Bueno-López, J. A. Anderson, *ACS Catal.* **2016**, *6*, 1723–1731.

Manuscript received: September 6, 2022
Revised manuscript received: November 13, 2022
Accepted manuscript online: November 15, 2022
Version of record online: December 8, 2022